

# Search for Dark Matter Particles via Invisible Decays in $^{46}\text{Sc}$ Nuclear Gamma Cascades with a CsI(Tl) Detector

Sharada Sahoo<sup>a</sup>, Jing-han Chen<sup>a</sup>, Mahdi Mirzakhani<sup>a</sup>, Harikrishnan Ramani<sup>b</sup>, Rupak Mahapatra<sup>a</sup>, Surjeet Rajendran<sup>c</sup>

<sup>a</sup>*Department of Physics and Astronomy, Texas A&M University, College Station, 77840, TX, US*

<sup>b</sup>*Physics and Astronomy, University of Delaware, Newark, Delaware, 19716, US*

<sup>c</sup>*Department of Physics and Astronomy, Johns Hopkins University, Baltimore, Maryland, 21218, US*

arXiv:2510.23001v3 [physics.ins-det] 11 Feb 2026

---

## Abstract

Dark matter remains one of the most compelling open problems in modern physics, motivating experimental searches for new light, weakly coupled particles beyond the Standard Model. Despite extensive efforts employing diverse detection strategies, large regions of parameter space remain unexplored. We report a high-statistics laboratory search for invisible decay modes in nuclear  $\gamma$ -ray cascades using approximately 100 kg of CsI(Tl) scintillators operated at Texas A&M University. The experiment employs a high-activity  $^{46}\text{Sc}$  radioactive source and a “missing- $\gamma$ ” technique, in which the absence of a photon from a well-identified cascade serves as a signature of new physics. Unlike appearance–disappearance experiments, this approach requires only a single photon conversion into a dark-sector particle, enabling sensitivity to significantly weaker couplings. The setup provides simultaneous sensitivity to a broad class of light dark-sector candidates, including axions and axion-like particles, dark scalars, and dark photons in the 0.1–1 MeV mass region. Through careful control of detector containment, energy resolution, and environmental backgrounds, we excluded certain regions on the previously explored parameter space. With foreseeable improvements in detector volume and systematic uncertainty control, this technique has the potential to probe currently unexplored parameter space for axion-like particles and light dark scalars.

---

## 1. Introduction

Various astrophysical observations based on the behavior of galaxies in the galaxy clusters [1, 2], rotational velocity curves of stars in galaxies [3], gravitational lensing [4], have confirmed the existence of non-luminous matter in the universe or the so-called dark matter. About 83% of the matter content of the universe is in the form of dark matter. This experiment aims to search for several dark matter candidates, including axions and axion-like particles (ALPs), dark scalars, dark photons, and milli-charged particles.

Light, weakly coupled particles below the MeV scale arise naturally in many extensions of the Standard Model and are compelling dark-sector candidates, either as dark matter itself or as mediators of its interactions. They also appear in solutions to the strong CP problem [5, 6, 7], the gauge hierarchy problem [8], and the cosmological constant problem [9], and have been invoked in astrophysical contexts such as stellar energy transport and supernova shock revival [10]. While astrophysical and cosmological observations place strong bounds on these particles, the limits are highly model-dependent and can be evaded with modest theoretical modifications. These considerations highlight the importance of laboratory-based searches with controlled systematics to provide robust and complementary probes of light, weakly coupled particles.

In this work, we present a high-statistic, laboratory-based search for rare invisible decay channels in well-identified nuclear gamma cascades. The experiment employs a  $^{46}\text{Sc}$  radioactive source placed at the center of a  $\sim 100$  kg CsI(Tl) scintilla-

tor array. By exploiting coincidence tagging of the 1120 keV gamma line and searching for the associated 889 keV photon, the setup is designed to identify missing gamma events that may signal the conversion of a photon into a hidden-sector particle such as an axion-like particle, dark photon, or scalar mediator. Through dedicated simulations, careful control of detector containment, and extensive background characterization using passive shielding and active vetoes, this work demonstrates the feasibility of probing rare processes in a controlled environment and sets the stage for next-generation ton-scale experiments with improved containment and sensitivity.

This paper is organized as follows. In Sec. II, we present the theoretical framework of the experiment, including the production of axions and axion-like particles (ALPs) from radioactive nuclear transitions, the resulting missing- $\gamma$  probability in the detector, and the overall sensitivity of the search. Section III describes the experimental setup, including the choice of radioactive sources, detector assembly, and the dominant backgrounds relevant to the measurement. The data acquisition system, detector characterization, stability of the experiment during data-taking, and the preliminary data analysis procedures are discussed in Sec. IV. In Sec. V, we present the analysis of the experimental results. Finally, Sec. VI summarizes the exclusion limits obtained for various dark-sector candidates, including axions and axion-like particles, dark scalars, dark photons, and milli-charged particles. This section also outlines potential upgrades and future improvements to the experimental setup aimed at enhancing the sensitivity and extending the search to

previously unexplored regions of parameter space.

## 2. Theoretical Framework

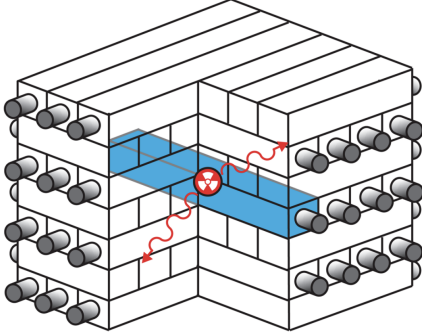


Figure 1: Experiment design [11]. Schematic diagram of the stacked CsI crystal assembly designed to efficiently contain  $\gamma$  rays emitted from the radioactive source positioned at its center.

Nuclear gamma cascades provide a clean and well controlled environment to search for exotic decay channels. Radioactive isotopes such as  $^{60}\text{Co}$  and  $^{46}\text{Sc}$  undergo beta decay followed by sequential gamma emissions as the daughter nucleus de-excites to its ground state. The resulting gamma spectra exhibit well defined and characteristic lines associated with each transition. Both isotopes feature two gamma lines, allowing one gamma to be used as a tag while the second is examined for anomalies. In practice, the large energy separation between the two gamma lines in  $^{46}\text{Sc}$  compared to  $^{60}\text{Co}$  makes  $^{46}\text{Sc}$  the preferred choice.

There are two generic mechanisms by which radioactive decays can produce dark sector particles. In the first, an intermediate excited nuclear state decays invisibly by emitting a dark sector particle instead of a gamma photon. In this case, the standard gamma cascade appears incomplete. In the second mechanism, a gamma emitted in the cascade subsequently converts into a hidden sector particle through suppressed but non zero interactions with surrounding nuclei or electromagnetic fields. Examples include axions or axion like particles produced via Primakoff type processes or related conversion channels. In both scenarios, the final state consists of one observed gamma and one beyond Standard Model particle, leading to an apparent missing gamma in an otherwise well understood two gamma cascade. This missing gamma signature provides a direct and experimentally robust handle to search for new physics.

This work focuses on a set of theoretically well-motivated models together with their effective interaction operators [12]. Table 1 summarizes the expressions for the missing branching fractions corresponding to different dark matter candidates. The parameter  $g_p$  denotes the effective scalar coupling to nucleons [11], while  $\phi$  represents a scalar mediator of mass  $m_\phi$ . The symbol  $\epsilon$  refers to the kinetic mixing parameter between the Standard Model photon and the dark photon fields, where the dark photon has mass  $m_{A'}$ . The parameter  $Q$  corresponds to the fractional electric charge of a milli-charged particle  $\chi$  with mass  $m_Q$ . Finally,  $a$  denotes an axion-like particle (ALP) whose coupling to photons is characterized by the decay constant  $f_{a\gamma}$ .

Table 1: Missing branching fractions of the dark matter candidates.

Model	$\mathcal{L}_{\text{int}}$	$\text{BR}_{\text{miss}}$
Scalar (nucleon coupling)	$g_p \phi \bar{N}N$	$\frac{g_p^2}{2e^2} \left(1 - \frac{m_\phi^2}{\omega^2}\right)^{5/2}$
Dark Photon	$\epsilon F^{\mu\nu} F'_{\mu\nu}$	$\epsilon^2 \left(1 - \frac{m_{A'}^2}{\omega^2}\right)^{5/2}$
Milli-charged Particle	$-Q \bar{\chi} \gamma^\mu A_\mu \chi$	$\frac{Q^2}{9} \frac{25\alpha}{\omega^5} \kappa(\omega, m_Q)$
ALP (photon coupling)	$\frac{1}{4f_{a\gamma}} a F_{\mu\nu} \tilde{F}^{\mu\nu}$	$\frac{\sigma_P}{\sigma_P + \sigma_{SM}} (1 - e^{-\ell/\lambda})$

The coupling constants  $g_p$ ,  $\epsilon$ ,  $Q$ , and  $f_{a\gamma}$  thus define the primary experimental parameters governing the sensitivity of the search to new physics beyond the Standard Model.

This approach offers an advantage over other laboratory-based axion searches, such as those using reactors or beam-dump experiments or light shining through the wall experiments. In our case, we focus solely on the production of rare particles at the source, without relying on their subsequent conversion back to photons or electrons at the detection site. As a result, the detection strategy requires only a single interaction during the nuclear decay itself thereby increasing the probability of observing such rare events.

## 3. Experimental set-up

Completing the experiment requires both the construction and detailed characterization of the detector. The proposed setup consists of a  $\sim 100$  kg CsI(Tl) scintillator array with a radioactive source placed at its center. The source is selected such that it undergoes decays that produce at least two particles: one acting as a trigger or tag, and the other providing sensitivity to potential rare or invisible decay modes.

The choice of radioactive isotope is therefore crucial. Common candidates such as  $^{24}\text{Na}$ ,  $^{60}\text{Co}$ , and  $^{46}\text{Sc}$  emit two primary  $\gamma$  rays suitable for coincidence measurements. Among these,  $^{46}\text{Sc}$  is particularly advantageous, as it emits well-separated  $\gamma$  lines at 889 keV and 1120 keV that can be clearly resolved by the detector. Its half-life of 84 days ensures a sufficiently long data-taking period, while the source activity can be tuned to provide high decay statistics without introducing excessive pile-up. These features make  $^{46}\text{Sc}$  a well-motivated choice for use with the CsI(Tl) detector. However, a key limitation of CsI(Tl) is its slow decay time ( $3\mu\text{s}$ ), which restricts the choice of source activity to  $< 1\mu\text{Ci}$  to prevent pile-ups in the data acquisition system.

### 3.1. Detector Assembly

CsI(Tl) is an excellent choice for gamma-ray detection because of its high density, which provides superior containment efficiency compared to other available scintillators. Moreover, our group has access to more than 10 tons of CsI (Tl) crystals, originally commissioned for the CLEO experiment [13].

The complete setup consists of 26 CsI (Tl) crystals (including 2 central halves), arranged in a  $5 \times 5$  square matrix to form



Figure 2: Detector Assembly with 100 Kg scale CsI (Tl) with attached PMTs.

a compact and symmetric detection volume (Fig.2). To suppress cosmic muon-induced background, a BC-400 plastic veto layer was added surrounding the scintillator array. Surrounding the entire detector and veto assembly, a 4-inch thick lead shield was installed to reduce the environmental  $\gamma$  background. Additionally, the setup is enclosed in a thermal insulation box maintained at a constant temperature of 70 °F to ensure stable PMT performance and minimize gain drift due to temperature fluctuations.

### 3.2. DAQ system

With the full shielding and cooling systems in place, the detector assembly is now fully operational and prepared for data collection using the radioactive source. High-voltage biasing for the photomultiplier tubes (PMTs) is provided by a CAEN SY5527LC mainframe equipped with two A7236 HV modules. Signal readout is performed with a CAEN V1740D digitizer installed in a compact CAEN VME mini-crate.

Data acquisition was performed using the CoPASS software optimized for the V1740D digitizer. Owing to the  $> 3 \mu\text{s}$  decay time of CsI(Tl) crystals [14], a total acquisition window of  $10 \mu\text{s}$  was used, with each waveform triggered at 40% of the window. The energy of each event was reconstructed by integrating the pulse amplitude over a  $3 \mu\text{s}$  window starting from the trigger point. CoPASS allows direct generation of energy spectra without storing individual waveforms, significantly reducing data volume. For offline analysis, it records in (CSV) format containing the channel number, trigger timestamp, and reconstructed deposited energy.

### 3.3. Backgrounds

Although the present search strategy is based on identifying a deficit in a well-defined gamma cascade rather than an excess of events, several sources of background can mimic a missing-gamma signature and must be carefully quantified. These backgrounds arise primarily from finite detector containment, environmental radiation, and intrinsic radioactive processes.

The dominant background arises from the finite gamma-ray containment of the detector. The  $^{46}\text{Sc}$  source is placed at the center of a  $\sim 100 \text{ kg}$  CsI(Tl) detector, providing a minimum path length of approximately 4 inches for each emitted gamma. However, the absorption efficiency of CsI(Tl) at 889 keV and 1120 keV is less than unity. Consequently, a fraction of otherwise standard cascade events will lose one gamma due to escape

from the active volume, producing an irreducible background. The detector containment efficiency is evaluated using detailed GEANT4 simulations by computing the fraction of events depositing energy within the region of interest (ROI).

Additional backgrounds arise from environmental radiation that can populate the ROI of the tagged gamma. These include intrinsic radioactive contaminants in the CsI(Tl) crystal and external sources such as ambient gamma rays, cosmic-ray-induced particles, and neutrons. Gamma rays with energies near the tagging line (around 1120,keV) are of particular concern, as they can lead to accidental coincidences. The combined background spectrum for the experimental setup is shown in

To suppress external backgrounds, the detector is enclosed within 10 cm (4 inches) of lead shielding. In addition, 11 plastic scintillators, each measuring  $14'' \times 4'' \times 2''$ , are deployed as an active veto layer surrounding the detector and positioned outside the lead shielding. This configuration significantly reduces backgrounds from ambient gamma rays and cosmic-ray-induced particles. Residual background contributions are characterized using dedicated background runs acquired without the radioactive source, providing a reference spectrum for the rare-event search. The resulting background spectrum, shown in Fig. 3, is used to estimate the environmental background rate in the region of interest (ROI). Combined with the detector containment efficiency obtained from simulation, this defines the total expected background in the experiment.

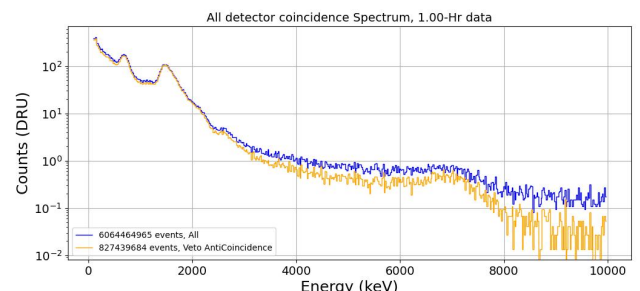


Figure 3: Energy spectra from CsI(Tl) without any external source, showing only the environmental background. The spectrum over 0–10 MeV is shown, where peaks at 660 keV ( $^{137}\text{Cs}$ ) and 1460 keV ( $^{40}\text{K}$ ) are visible. The blue line corresponds to the full background spectrum, while the orange line shows the single-scattered background spectrum.

## 4. Data Acquisition

Before proceeding to taking data with  $^{46}\text{Sc}$ , there are a few essential steps that need to be addressed such as detector characterization such as data linearity in the detected gamma energy, energy resolution at different gamma energy, energy threshold of the detector and also the stability data acquisition throughout the operation.

### 4.1. Detector Characterization

Each CsI(Tl) crystal was characterized for energy response, linearity, resolution, and effective trigger threshold using calibrated radioactive sources, including  $^{22}\text{Na}$ ,  $^{60}\text{Co}$ ,  $^{57}\text{Co}$ ,  $^{137}\text{Cs}$ ,

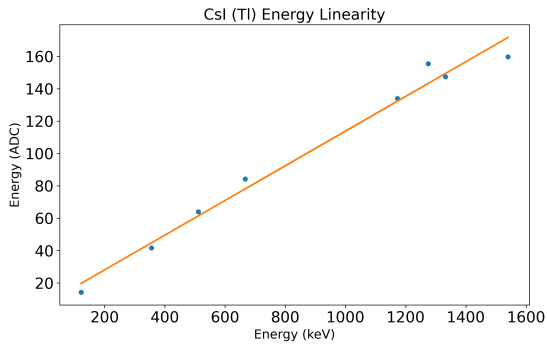


Figure 4

Figure 5: Energy characterization of a representative CsI (TI) crystal. Energy response tested using multiple radioactive sources ( $^{22}\text{Na}$ ,  $^{60}\text{Co}$ ,  $^{57}\text{Co}$ ,  $^{137}\text{Cs}$ , and  $^{133}\text{Ba}$ ) shows excellent linearity across the energy range 100 keV – 1600 keV.

and  $^{133}\text{Ba}$ . Gamma lines spanning 122–1460 keV were measured with the sources placed in direct contact with the crystals. The detectors exhibit a linear energy response over this range, demonstrating reliable performance of the crystal–PMT–base system for precision gamma spectroscopy (Fig. 5).

The detector exhibits linearity over the 0.1–2 MeV range, with an energy resolution of approximately 6%, ranking among the best values obtained with PMT-based systems. The threshold efficiency averages around 200 keV across all channels, providing sufficient confidence in deploying the detector for a  $^{46}\text{Sc}$  source–based missing  $\gamma$  search at 889 keV and 1120 keV. Additional details of these measurements are presented in Appendix 8.

#### 4.2. Detector Stability

Prior to extended data taking with the  $^{46}\text{Sc}$  source, detector stability was evaluated by monitoring the positions of calibration peaks as a function of time. A gain drift was observed during the first  $\sim 30$  minutes of operation, consistent with heating of the photomultiplier tube (PMT) base. The application of external cooling stabilized the base temperature and significantly improved the gain stability after a short warm-up period. The combination of active cooling and controlled data acquisition effectively mitigated PMT base overheating, enabling stable and reliable long-term detector operation.

#### 4.3. Preliminary data analysis with $^{22}\text{Na}$

The  $^{22}\text{Na}$  source was used to verify detector functionality and containment efficiency. In each  $^{22}\text{Na}$  decay, a positron is emitted in coincidence with a 1275 keV gamma ray. The positron subsequently annihilates with an electron, producing two additional 511 keV gamma rays, such that a single decay can yield up to three gammas. Although all three gamma rays are emitted nearly simultaneously on the nanosecond timescale [15], the corresponding detector triggers are spread over longer times due to the relatively long decay time of the CsI(Tl) scintillator [14] and the trigger efficiency of the digitizer. This makes

the choice of an appropriate time coincidence window a critical aspect of the analysis.

Based on a detailed study described in the Appendix 8, a coincidence window of  $0.5 \mu\text{s}$  was selected. All signals occurring within this window are grouped together and treated as originating from a single decay. In some cases, more than three signals are observed when one or more gamma rays undergo Compton scattering within the detector. Conversely, fewer signals may be recorded if gamma rays escape without interaction or deposit energy below the trigger threshold. Events with fewer than the expected number of signals constitute potential signal candidates and are discussed in detail in later sections.

Using the  $^{22}\text{Na}$  data, the experimental results were found to be in good agreement with expectations. A key diagnostic used for validating both detector performance and event reconstruction is the event multiplicity distribution, defined as the number of crystals triggered within a single decay event. This distribution peaks at a multiplicity of three, consistent with the emission of three gamma rays in the  $^{22}\text{Na}$  decay cascade, confirming the correct functioning of the detector system and analysis framework. In addition, the co-added energy spectrum, defined as the total energy deposited within a single decay, shows good agreement with simulation, providing further confidence to proceed with measurements using the  $^{46}\text{Sc}$  radioactive source. Additional details of the  $^{22}\text{Na}$  studies are provided in the Appendix 8.

## 5. Results and Analysis

A total of more than 1000 hours of data were collected using a  $^{46}\text{Sc}$  radioactive source with the CsI(Tl) detector array. However, a significant fraction of the data was rendered unusable due to failures in the photomultiplier tube (PMT) bases. These failures mostly arise due to overheating of resistors in the base, which prevented proper biasing of the PMT and resulted in a complete loss of signal in the affected channel, and leading to unlikely energy value. To overcome this, the affected data was discarded and the faulty bases were replaced. After applying strict data quality selection criteria, only slightly more than 100 hours of high-quality data were retained for the final analysis.

Monte Carlo simulations of the experiment were performed using the GEANT4 simulation toolkit developed by CERN, with assistance from a collaborator at Texas A&M University. The simulations accurately reproduce the experimental geometry and incorporate the radioactive source, detector energy thresholds, and energy-dependent energy resolution effects. The GEANT4 PhysicsList package is used to model particle interactions with matter, including electromagnetic interactions of electrons and photons with the matter. Additional details of the simulation framework are provided in the Appendix 8.

The event multiplicity distribution was constructed and is shown in Fig. 6. The distribution peaks at a multiplicity of two, consistent with the expected emission of two  $\gamma$  rays in the  $^{46}\text{Sc}$  decay cascade. This agreement confirms the proper functioning of both the detector system and the analysis framework. Events with multiplicity greater than two arise primarily from Compton scattering, in which a  $\gamma$  ray deposits energy in multiple de-

tector channels. Events with multiplicity equal to one define the signal region and include contributions from detector containment losses, environmental backgrounds, and potential exotic decay signatures. The composition of this region is quantified in the following sections.

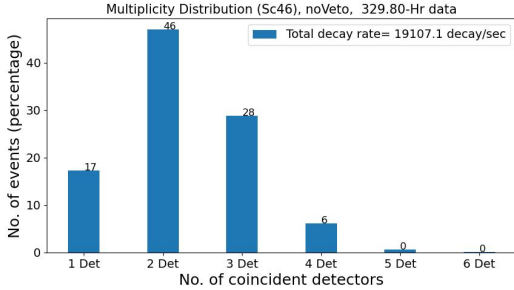


Figure 6: Multiplicity plot.

To more clearly identify potential missing-gamma events, we examine the co-added energy spectrum, defined as the total energy deposited across all detector crystals within a single decay. Good agreement is observed between data and Monte Carlo simulation, with a clear total-absorption peak at approximately 2 MeV (889 keV + 1120 keV), as well as single-gamma absorption peaks at 889 keV and 1120 keV (Fig. 7). The single-gamma peaks correspond to events in which one gamma ray is detected while the other escapes the detector volume, providing the baseline for the missing-gamma search.

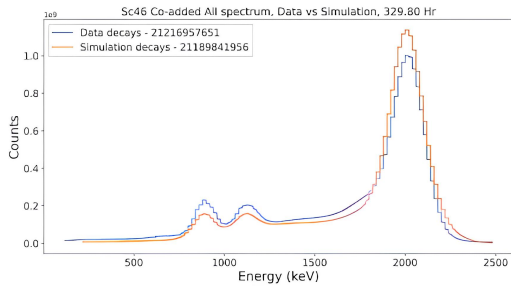


Figure 7: Co-added energy spectrum of  $^{46}\text{Sc}$  including all detector channels.

For the present analysis, the 1120 keV  $\gamma$  ray is used as the tagging photon, and the search is performed for the coincident 889 keV  $\gamma$  ray. This choice is motivated by two considerations. First, the 889 keV peak is susceptible to contamination from Compton-scattered 1120 keV events; using the 889 keV line as the tagging photon could therefore lead to misidentification of Compton-scattered 1120 keV  $\gamma$  rays as true cascade events. Second, the detector exhibits higher containment efficiency at 889 keV than at 1120 keV. Taken together, these considerations make the 1120 keV line the more reliable tagging channel for this analysis.

Figure 7 shows a clear discrepancy between data and simulation in the region of the 1120 keV single-gamma absorption peak (equivalently, the 889 keV escape peak). This excess indicates that a fraction of the missing 889 keV gamma events cannot be explained solely by detector containment inefficiency as

shown by the simulation spectrum.

The number of missing-gamma events is estimated by counting events within the  $1120 \pm 1.5\sigma$  region of the co-added energy spectrum across all channels, where the choice of  $1.5\sigma$  is motivated by the separation between the 889 keV and 1120 keV peaks. For a total exposure corresponding to  $7.54 \times 10^9$   $^{46}\text{Sc}$  decays, the data yield  $690.19 \pm 25.6 \times 10^6$  (9.15 %) missing-gamma events. The simulation predicts  $565.27 \pm 9.08 \times 10^6$  (7.49 %) events from standard processes, resulting in an excess of  $125.08 \pm 27.2 \times 10^6$  (1.65%) events not accounted for by detector containment alone. Additional contributions, such as residual external radioactive backgrounds not included in the simulation, may partially explain this excess. However, the estimated contribution from the background to the missing gamma events is  $4.16 \times 10^6$  (0.055 %). Which is insufficient to explain the observed discrepancy.

Further investigation identifies pile-up in the data acquisition (DAQ) system as an additional background source not included in the simulation. Each recorded waveform spans 10  $\mu\text{s}$  and consists of a 2  $\mu\text{s}$  pre-pulse region, a 3  $\mu\text{s}$  integration window used for energy reconstruction, and a  $\sim 5$   $\mu\text{s}$  post-pulse region. Only the 3  $\mu\text{s}$  integration window is used to identify and reconstruct an event. If a subsequent radioactive decay occurs within the post-pulse region of a triggered channel, one of the gamma rays from that decay may fall outside the integration window and therefore not be recorded. Such events can be misidentified as missing- $\gamma$  signatures in the subsequent trigger. Dedicated runs with modified acquisition settings are used to quantify this effect, indicating that approximately 0.95% of the observed missing- $\gamma$  events (with the 1120 keV photon used as the tagging gamma) are attributable to pile-up. This contribution accounts for the majority of the discrepancy observed between data and simulation, leaving a residual unexplained excess of approximately 0.65%.

Statistical and systematic uncertainties were evaluated using a cut-variation approach. Several analysis variables contribute to the uncertainty in the extracted signal. The systematic uncertainty associated with each variable was estimated by varying it around its nominal value and evaluating the resulting change in the missing- $\gamma$  count; the standard deviation of these variations was taken as the systematic uncertainty for that variable. This procedure was repeated for all variables that could affect the missing- $\gamma$  yield, and the total systematic uncertainty was obtained by summing the individual contributions in quadrature. The statistical uncertainty was determined independently and is given by the square root of the number of missing- $\gamma$  events in each case. Table 2 summarizes the missing- $\gamma$  fraction, the relevant background contributions, and the associated statistical and systematic uncertainties. More content regarding the uncertainties are explained in the Section 8.

The total systematic uncertainty was found to be 0.373%, while the total statistical uncertainty is negligible at  $< 0.001\%$ . The measured missing- $\gamma$  signal fraction is 0.65%, with a total uncertainty dominated by the systematic component.

Table 2: Summary of missing gamma contributions and associated uncertainties. Numbers are given relative to the total  $7.54 \times 10^9$  decays, with percentages in parentheses.

Category	Number ( $\times 10^6$ ) (%)	Systematic (%)	Statistical (%)
Total Decay	7542.8 (100)	–	–
Missing gamma events – data (Tag 1120 keV)	690.19 (9.15)	0.34	0.00035
Containment Inefficiency (Simulation)	565.27 (7.49)	0.12	0.00031
Pile-up (in the ROI at 889 keV)	70.53 (0.94)	0.01	0.0001
Radioactive background	4.16 (0.055)	0.001	0.00003
BRICC (Conversion electron from a decay)	1.21 (0.016)	theoretical	0.00001
<b>Remaining excess</b>	<b>49.04 (0.65)</b>	<b>0.373</b>	<b>&lt; 0.001</b>

## 6. Conclusion And Experimental Reach

The statistical significance of the observed excess was evaluated using the test statistic

$$Z = \frac{S}{\sigma_{\text{total}}}, \quad (1)$$

where the total uncertainty is defined as

$$\sigma_{\text{total}} = \sqrt{\sigma_{\text{stat}}^2 + \sigma_{\text{sys}}^2}. \quad (2)$$

Using the number of decays, the estimated backgrounds, and the systematic uncertainties discussed above, the resulting significance is

$$Z = 1.73.$$

This value falls well below the conventional thresholds typically used in rare-event searches:  $Z > 5$  corresponds to a discovery claim, while  $Z > 3$  is considered evidence for a possible signal. Thus, the present measurement does not indicate a statistically significant deviation attributable to new physics.

Table 3: Exploration for parameter space for different Dark-Matter candidates such as Dark Scalar, Dark Photon and ALPs.

Candidates	Mass (MeV)	Coupling Constant	Present Limit	Future Limit
Dark Scalar	0.1 - 1	$g_p$	$> 8e - 2$	$> 1e - 8$
Dark Photon	0.1 - 1	$\epsilon$	$> 1e - 1$	$> 1e - 8$
ALP	0.1 - 1	$f_{ay}(GeV^{-1})$	$> 6e - 1$	$> 1e - 7$

With the first generation of the experiment, we probed a portion of the parameter space for axion-like particles (ALPs), scalar dark matter, and dark photons, demonstrating the sensitivity and potential of this technique for searches beyond the Standard Model. The exclusion limits were derived using the expressions listed in Tab. 1 and are shown in Fig. 8. The next generation of the experiment is expected to further extend this sensitivity, enabling coverage of regions of parameter space that remain unexplored by existing experiments. The ranges of parameter space investigated in this work are summarized in Tab. 3.

The primary limitations of the present experiment arise from limited gamma-ray containment and relatively large systematic

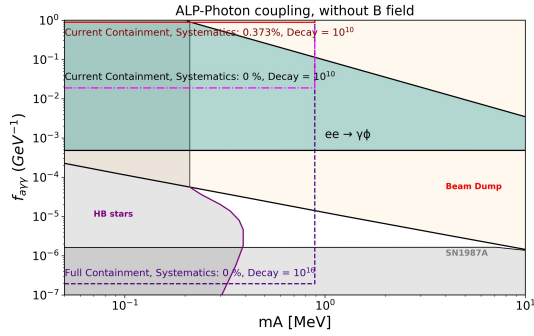
uncertainties, which motivate the design of the next-generation upgrade. An upgraded, ton-scale experiment is currently under development and is expected to extend the sensitivity into previously unexplored regions of parameter space, including the cosmological triangle for axion-like particles (ALPs) and broad, untested regions for scalar dark matter. This study highlights the importance of reducing systematic uncertainties, which are dominated by the energy threshold and the choice of coincidence window. The energy threshold is strongly influenced by the use of photomultiplier tubes (PMTs), whose gain instabilities can lead to threshold fluctuations; replacing PMTs with silicon photomultipliers (SiPMs) is expected to provide improved gain stability and enable lower, more uniform thresholds. In addition, systematic uncertainties associated with the coincidence window can be further reduced through optimized analysis strategies and faster data processing using C++-based algorithms.

Additional upgrades under consideration include the use of high-purity CsI crystals with faster decay time ( $\sim 20$  ns), which could increase statistics by up to two orders of magnitude, and the deployment of auxiliary  $\beta$  detectors to improve tagging efficiency and coincidence rejection. Together, these developments will lay the foundation for the next-generation program aimed at exploring rare processes in nuclear gamma cascades with unprecedented sensitivity. Furthermore, alternative radioactive sources such as  $^{90}\text{Nb}$ ,  $^{60}\text{Co}$ , and  $^{24}\text{Na}$  are being evaluated as substitutes for  $^{46}\text{Sc}$  to probe different dark matter mass ranges and other dark sector candidates [12].

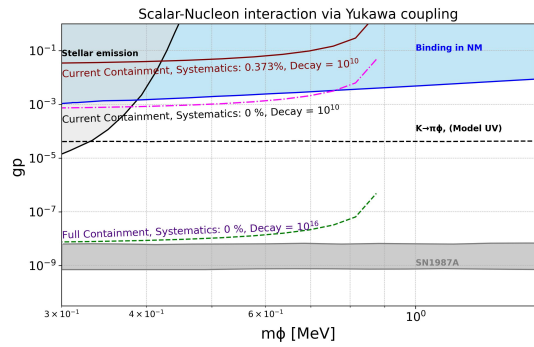
The detector is also being relocated to Los Alamos National Laboratory (LANL) to facilitate axion searches in a beam dump environment. A similar detector setup is planned for deployment at Oak Ridge National Laboratory (ORNL) to operate in the HFIR 85 MW reactor. This versatile detector system is designed to be compatible with a wide range of dark matter search environments, including reactor-based, beam-dump, and radioactive source experiments.

## 7. Acknowledgements

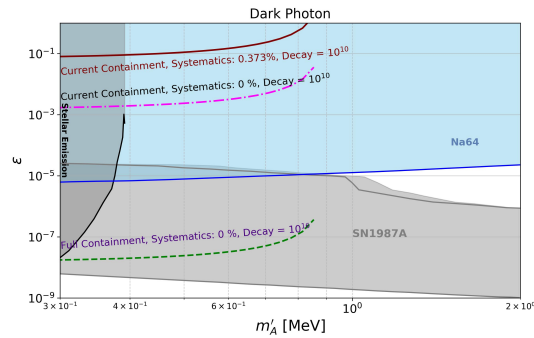
The work presented in this paper has been supported by LANL - TRIAD and DOE Grant Nos DE-SC0018981. We also acknowledge Mitchell Institute and the Nuclear Science and Engineering Center for providing institutional support with



(a) ALPs



(b) Scalar Dark Matter



(c) Dark Photon

Figure 8: Exclusion limits for different dark-sector models: (a) ALPs, (b) scalar dark matter, and (c) dark photons. The solid line denotes the currently excluded parameter space. The dash-dot line indicates the projected sensitivity achievable with improved control of systematics, while the dashed line corresponds to the projected reach of a future ton-scale detector with both improved systematics.

lab space and other required facilities to carry out experimentation.

## References

[1] F. Zwicky, Die Rotverschiebung von extragalaktischen Nebeln, *Helv. Phys. Acta* 6 (1933) 110–127. doi:10.1007/s10714-008-0707-4.

[2] F. Zwicky, 107. On the Masses of Nebulae and of Clusters of Nebulae, Harvard Univer-

sity Press, Cambridge, MA and London, England, 1979, pp. 729–737 [cited 2024-05-27]. doi:doi:10.4159/harvard.9780674366688.c115. URL <https://doi.org/10.4159/harvard.9780674366688.c115>

- [3] V. C. Rubin, J. W. K. Ford, Rotation of the andromeda nebula from a spectroscopic survey of emission regions, *Astrophys. J.* 159 (1970) 379–403.
- [4] C. Alcock, C. W. Akerlof, R. Allsman, T. Axelrod, D. Bennett, S. Chan, K. Cook, K. C. Freeman, K. Griest, S. L. Marshall, et al., Possible gravitational microlensing of a star in the large magellanic cloud, *nature* 365 (6447) (1993) 621–623.
- [5] R. D. Peccei, H. R. Quinn, Constraints imposed by CP conservation in the presence of pseudoparticles, *Phys. Rev. D* 16 (1977) 1791–1797. doi:10.1103/PhysRevD.16.1791. URL <https://link.aps.org/doi/10.1103/PhysRevD.16.1791>
- [6] S. Weinberg, A new light boson?, *Phys. Rev. Lett.* 40 (1978) 223–226. doi:10.1103/PhysRevLett.40.223. URL <https://link.aps.org/doi/10.1103/PhysRevLett.40.223>
- [7] F. Wilczek, Problem of strong  $p$  and  $t$  invariance in the presence of instantons, *Phys. Rev. Lett.* 40 (1978) 279–282. doi:10.1103/PhysRevLett.40.279. URL <https://link.aps.org/doi/10.1103/PhysRevLett.40.279>
- [8] P. W. Graham, D. E. Kaplan, S. Rajendran, Cosmological relaxation of the electroweak scale, *Physical Review Letters* 115 (22) (Nov. 2015). doi:10.1103/physrevlett.115.221801. URL <http://dx.doi.org/10.1103/PhysRevLett.115.221801>
- [9] P. W. Graham, D. E. Kaplan, S. Rajendran, Relaxation of the cosmological constant, *Physical Review D* 100 (1) (Jul. 2019). doi:10.1103/physrevd.100.015048. URL <http://dx.doi.org/10.1103/PhysRevD.100.015048>
- [10] K. Mori, T. Takiwaki, K. Kotake, S. Horiuchi, Shock revival in core-collapse supernovae assisted by heavy axionlike particles, *Phys. Rev. D* 105 (6) (2022) 063009. arXiv:2112.03613, doi:10.1103/PhysRevD.105.063009.
- [11] J. B. Dent, B. Dutta, A. Jastram, D. Kim, A. Kubik, R. Mahapatra, S. Rajendran, H. Ramani, A. Thompson, S. Verma, Pathfinder for a high statistics search for missing energy in gamma cascades, *Physical Review D* 105 (1) (Jan. 2022). doi:10.1103/physrevd.105.015030. URL <http://dx.doi.org/10.1103/PhysRevD.105.015030>

- [12] G. Benato, A. Drobizhev, S. Rajendran, H. Ramani, Invisible decay modes in nuclear gamma cascades, Phys. Rev. D 99 (2019) 035025. doi:10.1103/PhysRevD.99.035025. URL <https://link.aps.org/doi/10.1103/PhysRevD.99.035025>
- [13] E. Blucher, B. Gittelmann, B. K. Heltsley, J. Kandaswamy, R. V. Kowalewski, Y. Kubota, N. B. Mistry, S. Stone, A. Bean, Tests of Cesium Iodide Crystals for an Electromagnetic Calorimeter, Nucl. Instrum. Meth. A 249 (1986) 201. doi:10.1016/0168-9002(86)90669-8.
- [14] GammaData, Csi(tl) and na scintillation material data sheet, <https://gammadata.se/wp-content/uploads/2024/01/CsITl-and-Na-data-sheet-v2.pdf>, technical datasheet (2024).
- [15] S. R. Cherry, J. A. Sorenson, M. E. Phelps, Physics in Nuclear Medicine, 4th Edition, Elsevier, 2012.

## 8. Appendices

### 8.1. Detector Characterization

The energy linearity of the detector is discussed in the previous sections. Here, we present the energy-dependent detector resolution and the effective hardware trigger thresholds.

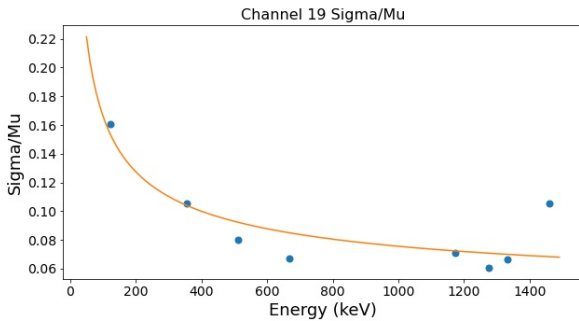


Figure 9: Relative energy resolution,  $\sigma/\mu$ , as a function of deposited energy. The resolution follows the expected scintillator behavior, scaling approximately as  $1/\sqrt{N}$ , where  $N$  is the number of collected scintillation photons.

The measured energy resolution follows the expected behavior for scintillation detectors, with  $\sigma/\mu \propto 1/\sqrt{N}$ , and is well described by this model over the full range of measured energies, as shown in Fig. 9.

The effective hardware trigger thresholds exhibit an error-function-like turn-on behavior. The majority of channels are clustered around thresholds of approximately 200 keV, with a small number of channels showing higher thresholds near 500 keV or lower thresholds near 100 keV (Fig. 10). Since the characteristic  $\gamma$ -ray energies from the  $^{46}\text{Sc}$  source lie well above this threshold region, the detector operates with high efficiency for the signals of interest. This provides confidence in the suitability of the radioactive-source-based axion and light dark-sector search using the present experimental setup.

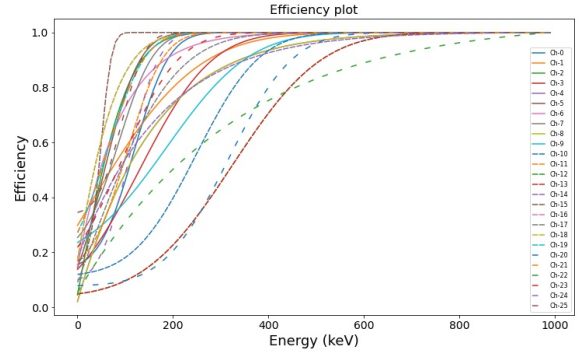


Figure 10: Effective hardware trigger thresholds for all detector channels. Most channels reach full collection efficiency at approximately 200 keV.

### 8.2. Estimation of Time Coincidence Window

To associate all signals originating from a single physical decay, a coincidence window is defined in the analysis. Events occurring within this window are grouped together and treated as a single decay event, ensuring that correlated multi-hit signals are not mistakenly identified as independent events.

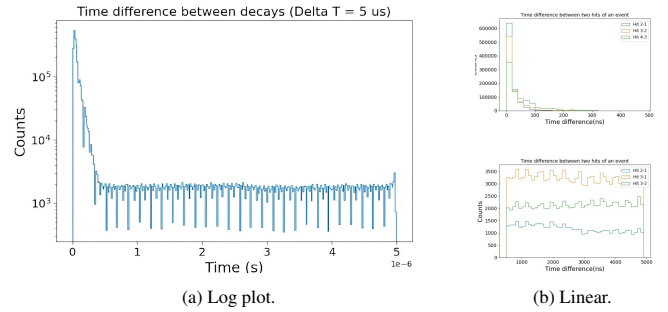


Figure 11: Histogram of time differences between consecutive events. A clear slope is observed within  $0.5 \mu\text{s}$ , representing the radioactive decay events while a flat spectrum beyond that representing background events.

The distribution of time differences between successive hits exhibits a pronounced excess at small time separations, indicating correlated signals from the same decay, while at larger separations the distribution becomes flat, consistent with uncorrelated background events.

Taking into account the observed clustering of events (Fig. 11) below  $0.5 \mu\text{s}$ , the digitizer time resolution (16 ns), the CsI(Tl) decay time constant ( $\sim 3 \mu\text{s}$ ), and empirical observations of pulse rise times, a coincidence window of  $0.5 \mu\text{s}$  was selected as a reasonable criterion for event grouping. Any potential loss of correlated events falling outside this window was treated as a systematic uncertainty and included in the final analysis.

### 8.3. Preliminary Analysis with $^{22}\text{Na}$

With a coincidence window of  $0.5 \mu\text{s}$  and a previously defined energy threshold of 100 keV applied to all channels, a multiplicity analysis was performed. The multiplicity distribution obtained using the  $^{22}\text{Na}$  source shows a clear peak at multiplicity three, where multiplicity is defined as the number of

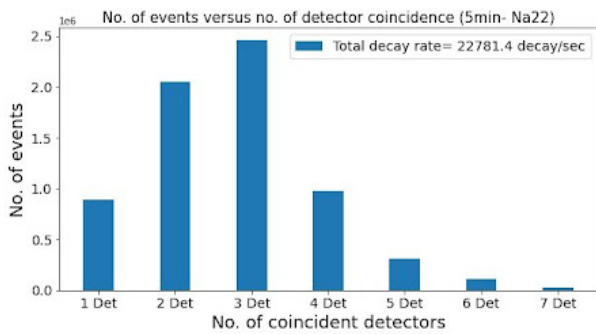


Figure 12: Multiplicity using  $^{22}\text{Na}$ .

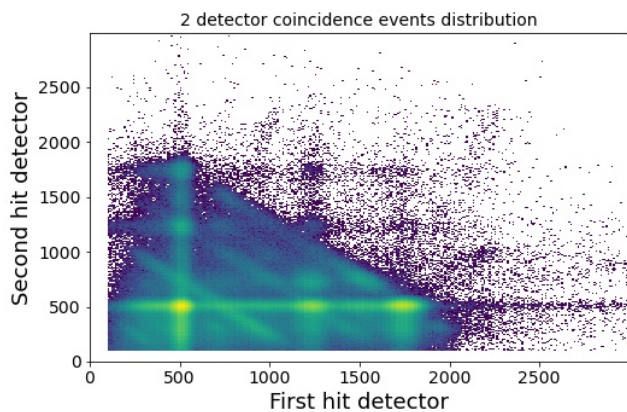


Figure 13: 2 detector event shared energy spectrum.

channels (or crystals) that trigger within the  $0.5 \mu\text{s}$  coincidence window. This behavior is consistent with the emission of three gamma photons per  $^{22}\text{Na}$  decay and validates the detector assembly, the time-coincidence grouping strategy, and the overall data acquisition and reconstruction framework.

A more detailed examination was performed for events within each multiplicity category shown in Fig. 12, beginning with **two-detector events**, defined as cases in which exactly two crystals triggered within the coincidence window. Figure 13 shows a two-dimensional histogram of the energy deposited in the first triggered detector versus that in the second triggered detector. Distinct clusters are observed at the expected energy combinations (511, 511), (511, 1275), (511, 1786), (1275, 511), and (1786, 511) keV, corresponding to the possible gamma-ray combinations produced in  $^{22}\text{Na}$  decays.

In addition to these clusters, diagonal bands are visible at total energies of 1275 keV, 1786 keV, and 2297 keV, indicating events in which a gamma ray shares its energy between two detectors, most likely through Compton scattering or partial energy deposition. A slight asymmetry is also observed in the distribution, with brighter clusters associated with the first triggered detector. This effect arises because higher-energy gamma rays, such as those at 1275 keV or 1786 keV, tend to produce faster-rising pulses that cross the digitizer threshold earlier, making them more likely to be recorded as the first trigger in the detector pair.

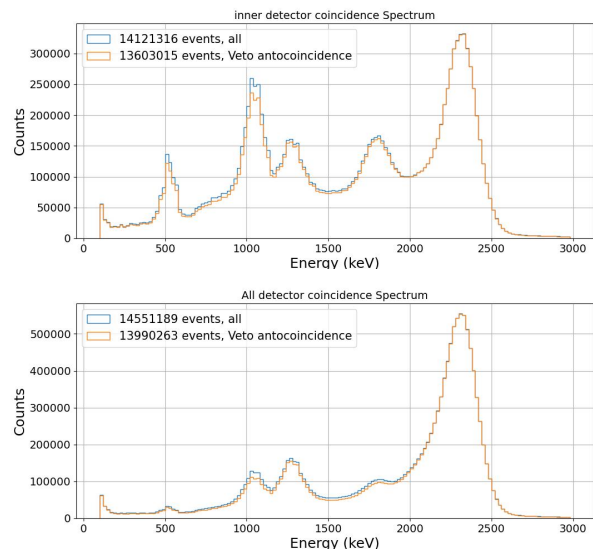


Figure 14: Co-added energy spectrum: inner  $3 \times 3$  detector and all  $5 \times 5$  detector.

The co-added energy spectrum provides a useful measure of the total gamma-ray energy contained within the detector and is defined as the sum of all signal energies recorded within the selected coincidence window. As shown in Fig. 14, the left panel corresponds to events reconstructed using only the inner  $3 \times 3$  region of the detector array, while the right panel includes the full detector volume.

The peak at 2297 keV corresponds to full energy absorption of all three gamma rays (1275 keV + 511 keV + 511 keV). The remaining peaks arise from partial energy containment and correspond to escape events. For example, the 511 keV peak represents events in which only a single 511 keV gamma is detected, with both the 1275 keV gamma and the second 511 keV gamma escaping the detector. The 1022 keV peak corresponds to events where only the two 511 keV gammas are detected, while the 1275 keV peak can arise either from escape of both 511 keV gammas or from the alternate  $^{22}\text{Na}$  decay branch that emits only a single 1275 keV gamma. The 1786 keV peak corresponds to events in which one 511 keV gamma escapes. As the effective detector volume increases, the escape peaks are suppressed and the total absorption peak becomes more prominent, consistent with improved gamma-ray containment in a larger detector.

#### 8.4. Simulation using GEANT4

As discussed in the previous sections, the detector response is modeled using the GEANT4 PhysicsList package. Figure 15 shows the simulated experimental setup. Due to the unavailability of an image of the full detector assembly, a reduced  $3 \times 3$  configuration is shown for illustration, while all analyses are performed using simulations of the full  $5 \times 5$  detector geometry.

The validity of the simulation framework is further assessed by comparing simulated and experimental energy spectra for individual detector channels.

Figure 16 demonstrates good agreement between simulation and data after applying detector resolution and threshold effects. In particular, the two characteristic gamma-ray peaks

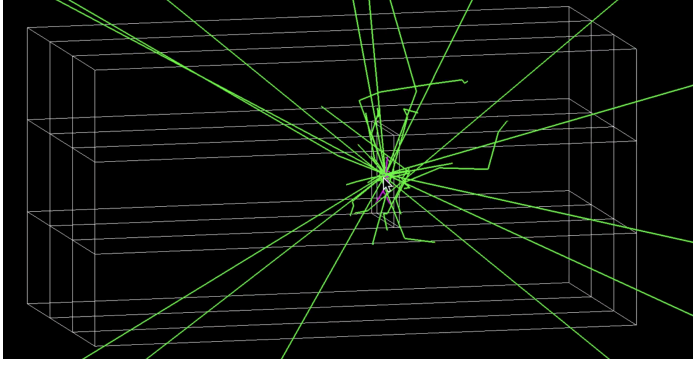


Figure 15: Simulation of the experimental setup. A reduced  $3 \times 3$  version of the detector is shown. The radioactive source is placed at the center, emitting gamma rays (green) and beta particles (pink).

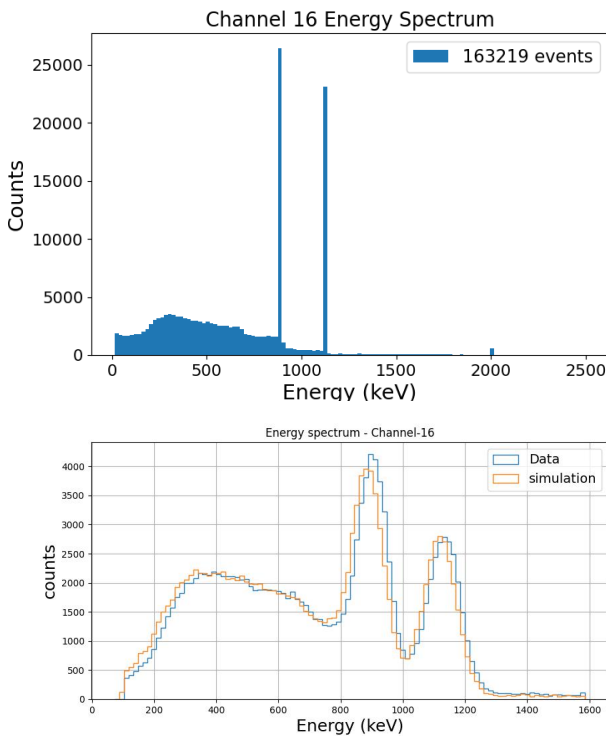


Figure 16: Energy spectrum for detector Channel 16. The left panel shows the raw simulated spectrum, while the right panel shows the spectrum after applying detector resolution and threshold efficiency, compared with experimental data.

from  $^{46}\text{Sc}$  are well reproduced. This agreement provides confidence in the simulation framework and justifies its use in estimating the detector containment efficiency.

## 8.5. Errors and Uncertainty

Several sources of error and uncertainty must be evaluated in this experiment. In general, experimental uncertainties can be categorized into two types:

- **Statistical uncertainty:** This quantifies the uncertainty arising from finite data samples and random fluctuations, and it decreases as the amount of collected data increases.

- **Systematic uncertainty:** This arises from potential biases in the experimental setup and analysis procedures.

### 8.5.1. Calculation of Statistical Uncertainty

The statistical uncertainty is straightforward to estimate. For the large data sets considered in this analysis, the statistical fluctuations are well described by a Gaussian distribution and given by the square root of the number of events in each case.

$$\sigma_{\text{stat}} = \sqrt{\sum_i \sigma_{\text{stat}, B_i}^2}$$

$$\sigma_{\text{stat}, B_i} = \sqrt{N_{B_i}}$$

Where:

- $\sigma_{\text{stat}, B_i}$ : Statistical uncertainty from the  $i^{\text{th}}$  background source.
- $N_{B_i}$ : Number of missing gamma counts from the background source  $i^{\text{th}}$ .

Table 4: Estimated statistical uncertainties in the missing gamma contributions.

Category	Number ( $\times 10^6$ )	Statistical Uncertainty (%)
Total Decays	7542.8	
Data	690.19	$3.5 \times 10^{-4}$
Simulation	565.27	$3.1 \times 10^{-4}$
Pile-up Contribution	70.53	$1 \times 10^{-4}$
Background Contribution	4.16	$3 \times 10^{-5}$
BRICC Process	1.21	$1 \times 10^{-5}$
<b>Excess (Unaccounted)</b>	<b>49.04</b>	<b>&lt; 0.001%</b>

### 8.5.2. Calculation of Systematic Uncertainty

There are multiple sources of systematic uncertainties computed for the experiment. But I have outlined some of the highest contributing factors.

#### Coincidence window selection:

The choice of the coincidence window is one of the most critical factors influencing the overall systematic uncertainty of the analysis. A coincidence window of  $0.5 \mu\text{s}$  was selected to group events originating from a single decay, with all subsequent triggers within this interval treated as part of the same decay sequence. An inaccurate choice of this window can significantly affect the extracted missing- $\gamma$  fraction.

To estimate the associated systematic uncertainty, the coincidence window was varied to  $0.4 \mu\text{s}$ ,  $0.45 \mu\text{s}$ ,  $0.5 \mu\text{s}$ ,  $0.55 \mu\text{s}$ , and  $0.6 \mu\text{s}$ , and the full analysis chain was repeated for each case. Owing to computational constraints, this study was carried out using a representative 15-minute subset of the data. The resulting spread in the number of missing- $\gamma$  events was quantified, and the standard deviation was taken as the systematic uncertainty. This corresponds to a standard deviation of 3217.15 events, or 0.058%, relative to a total of 5,517,417 decay events in the 15-minute data set.

Table 5: Event counts as a function of coincidence time window.

Time Window ( $\mu\text{s}$ )	Missing gamma Counts
0.40	525088
0.45	522753
0.50	520570
0.55	518348
0.60	515918

### Energy threshold:

A similar procedure was followed to evaluate the systematic uncertainty associated with the software energy threshold. The analysis was repeated with threshold values of 60 keV, 80 keV, 100 keV, 120 keV, and 140 keV. The resulting variation in the missing- $\gamma$  counts at the end of the analysis pipeline was used to quantify the associated uncertainty. The standard deviation of the missing- $\gamma$  counts is 14,749.84 events, corresponding to 0.267% of the total 5,517,417 decay events in the 15-minute data set.

Table 6: Event counts as a function of energy threshold.

Energy Threshold (keV)	Counts
60	550392
80	550080
100	520570
120	520073
140	519757

### Calibration shifts:

Energy calibration for all detector channels was performed using an automated procedure that smooths the energy spectrum and identifies the first peak in the  $^{46}\text{Sc}$  spectrum. In some cases, the identified peak position deviates by 1–2 ADC bins from the true peak, which can affect the extracted missing- $\gamma$  yield.

To estimate the associated systematic uncertainty, the calibration peak for each channel was manually shifted by  $\pm(1-2)$  ADC bins relative to the automatically determined position, and the full analysis pipeline was repeated for each variation. The resulting spread in the missing- $\gamma$  counts was used to determine the systematic uncertainty due to calibration shifts. The individual channel contributions were then combined using a weighted quadrature sum,

$$\text{Total uncertainty} = \sqrt{\sum_i p_i \cdot \sigma_i^2}, \quad (3)$$

where  $p_i$  is the relative probability of each channel contributing to the detected events and  $\sigma_i$  is the corresponding channel-wise systematic uncertainty. The total systematic uncertainty from calibration shifts was found to be 0.21%.

### Variation of the detector resolution:

Detector energy resolution is an important input to the simulation and can influence the estimated contribution of missing- $\gamma$  events. The resolution was characterized by evaluating  $\sigma/\mu$  at

multiple energies using calibrated radioactive sources and fitting these values with a resolution model. Variations in the fitted parameters modify the simulated energy spectra for individual channels and can therefore affect their contribution to the missing- $\gamma$  signal.

To quantify this effect, the resolution-function parameters were varied by sampling Gaussian random distributions defined by the fit covariance matrix (Fig. 17). This procedure induces small shifts in the simulated energy response, as observed in the co-added energy spectrum for individual channels, and was repeated independently for all channels. The resulting variations in the missing- $\gamma$  counts were used to estimate the corresponding systematic uncertainty.

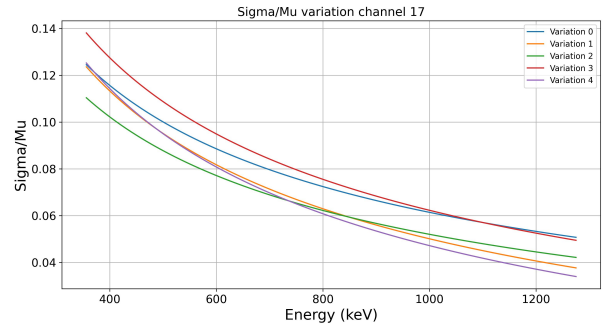


Figure 17: Variation of  $\sigma/\mu$  for one channel.

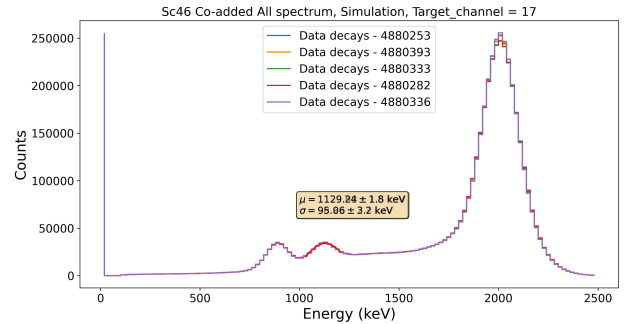


Figure 18: Effect of  $\sigma/\mu$  variation on the total co-added energy spectrum (right).

As in the previous cases, the channel-wise uncertainties were combined using a weighted quadrature sum,

$$\text{Total uncertainty} = \sqrt{\sum_i p_i \cdot \sigma_i^2},$$

where  $p_i$  is the relative contribution of each channel to the total number of detected events and  $\sigma_i$  is the systematic uncertainty in the missing- $\gamma$  yield for that channel. The total systematic uncertainty arising from detector resolution variations was found to be 0.12%.

Combining all the total systematic uncertainty was found to be 0.373%.